Journal of Power Sources 196 (2011) 6440–6448

Contents lists available at ScienceDirect

Journal of Power Sources

journal homepage: www.elsevier.com/locate/jpowsour

De-intercalation of $Li_xCo_{0.8}Mn_{0.2}O_2$: A magnetic approach

H.A.M. Abuzeid[a,*], A.M.A. Hashem[a], A.E. Abdel-Ghany[a], A.E. Eid[a], A. Mauger[b], H. Groult[c], C.M. Julien[c]

[a] Inorganic Chemistry Department, National research Centre, Behoss Street, Dokki, Cairo, Egypt
[b] Université Pierre et Marie Curie-Paris6, Institut de Minéralogie et Physique de la Matière Condensée, 4 place Jussieu, 75005 Paris, France
[c] Université Pierre et Marie Curie-Paris6, PECSA, 4 place Jussieu, 75005 Paris, France

ARTICLE INFO

Article history:
Received 20 December 2010
Received in revised form 4 March 2011
Accepted 26 March 2011
Available online 6 April 2011

Keywords:
$LiCo_{0.8}Mn_{0.2}O_2$
Li-batteries
Chemical delithiation
Magnetic properties

ABSTRACT

Samples of $LiCo_{0.8}Mn_{0.2}O_2$ were synthesized by a wet-chemical method using citric acid as a chelating agent, and were characterized by various physical techniques. Powders adopted the α-$NaFeO_2$ layered structure and were analyzed by X-ray diffraction (XRD), Fourier transform infrared spectroscopy (FTIR), and regarding their magnetic properties. Transmission Electron Microscope (TEM) revealed particles with a mean size of 100 nm. Partial chemical delithiation was carried out by using an oxidizing agent. We observe that the material has ability to free lithium ions from its structure by this chemical process, which is analogous to the first step of the charge transfer process in an electrochemical cell. The rate of delithiation is determined independently by magnetic measurements and by the Rietveld refinement of the XRD spectra. Both the concentration of Mn^{3+}–Mn^{4+} pairs and that of Mn^{4+}–Mn^{4+} pairs formed in the delithiation process have been determined, together with that of the Mn^{3+}–Mn^{3+} pairs. It shows that magnetic measurements are able to probe the distribution of Mn^{3+} and Mn^{4+} with more details than other techniques. The results are consistent with FTIR spectra, and indicate a random distribution of the Li ions that are removed from the matrix upon delithiation, which then undergo a diffusion process. Testing the material as cathode in lithium batteries revealed about 170 mAh g^{-1} capacity, with a lower polarization and a high columbic efficiency, emphasizing the possibility of using this material as a cathode in Li-ion batteries.

1. Introduction

Many compounds involving only one single transition metal element have been extensively studied as active cathode materials since a long time [1–7]. However, mixing metal ions is needed to optimize the stability and the electrochemical performance of the cathodes. $LiCo_{1-x}M_xO_2$ (M = Ni or Mn) [8–11] or mixtures of both [12–21] have been studied. They retain high capacity but also improve the cycling performance and thermal stability, while reducing the cost due to less content of the expensive Co.

$LiCo_{1-y}Mn_yO_2$ ($0 < y \leq 1$) samples have been prepared by Stoyanova et al. [19] by a solid-state reaction between LiOH and Mn–Co oxide spinels at 800 °C. These solid solutions have trigonal lattice for $y < 0.2$, are cubic in the range $0.2 < y < 0.7$, and crystallize in the tetragonal spinel structure in the compositional range $x > 0.7$. The best electrochemical properties, however, are obtained for $y < 0.7$. More recently, a sol–gel process was also used to prepare $LiCo_{1-y}Mn_yO_2$ for $y = 0.2$ [22].

In the present work we report the synthesis, physico-chemical characterization and electrochemical features of $LiCo_{0.8}Mn_{0.2}O_2$ for its potential use as a new generation cathode material for lithium-ion batteries. The synthesized $LiCo_{0.8}Mn_{0.2}O_2$ material and its delithiated phase obtained by chemical delithiation were characterized by conventional techniques, such as X-ray powder diffraction (XRD), and transmission electron microscope (TEM) images. Fourier transform infrared (FTIR) spectroscopy was used to probe the material at the mesoscopic scale. To examine the material at the atomic scale, however, we investigated the magnetic properties. Indeed, the difference between the spins carried by the Mn^{3+} and the Mn^{4+} ions generated by the delithiation process results in a dramatic dependence of the magnetic response of $Li_xCo_{0.8}Mn_{0.2}O_2$ on the rate x of delithiation. We took advantage of this effect to determine from the analysis of the magnetic properties, not only the concentration of Mn^{4+} ions, which is in quantitative agreement with the result of the Rietveld refinement of the XRD spectra, but also the pairing of Mn^{4+} ions with nearest Mn^{4+} and Mn^{3+} neighbors, an information on the distribution of the manganese ions that cannot be reached by other techniques. As a result, we found that the chemical process used for the delithiation allows only the manganese to oxide, thus limiting the value of x that can be reached. The electrochemical features of the oxide have been studied by coupling

* Corresponding author. Tel.: +33 144274439; fax: +33 144273882.
E-mail address: alain.mauger@impmc.jussieu.fr (H.A.M. Abuzeid).

0378-7753/$ – see front matter © 2011 Elsevier B.V. All rights reserved.
doi:10.1016/j.jpowsour.2011.03.054

it with Li anode in a non-aqueous electrolyte, and the electrochemical performance is discussed in relation to the results of the analysis of the FTIR results and these magnetic properties.

2. Experimental

2.1. Sample preparation

$LiCo_{0.8}Mn_{0.2}O_2$ powders were synthesized using a sol–gel technique described elsewhere [22]. This method involves the mixing of acetates of Li, Mn and Co, with citric acid (Fluka, MicroSelect grade) as complexing agent, mixed and dissolved in triple distilled water. By reacting appropriate molar ratios of hydrated metal acetates, i.e. $Li(CH_3COO)\cdot H_2O$ (Fluka), $Co(CH_3COO)_2\cdot 4H_2O$ (Fluka), $Mn(CH_3COO)_2\cdot 4H_2O$ (Fluka), a gel was formed. The carboxylic acid groups could provide chemical bonds with metal ions to form a viscous resin on evaporation of the solvent, which is usually called a precursor. The resultant solution was then evaporated off at 80 °C with magnetic stirring for about 6 h until a sol was formed. The resulting xerogel was transparent violet in color. Finally, the products referred as precursor powders were formed by heating the gel at 120 °C. It is a fluffy dark brownish powder. The decomposed powders were slightly ground and further heated to 400 °C in air to convert the metal carboxylates to oxides. The resulting products were sintered at 800 °C in air for 24 h. We have determined that this temperature is needed to form a single-phase $LiCo_{0.8}Mn_{0.2}O_2$, with complete hexagonal ordering. The products obtained were fine-grained materials of submicron-sized particles.

2.2. Apparatus

The crystal structure of the prepared samples was analyzed by X-ray diffractometry (XRD) using Philips X'Pert apparatus equipped with a Cu Kα X-ray source (λ = 1.5406 Å). XRD measurements were collected in the 2θ range 10–80°. FTIR spectra were recorded with Bruker IFS 113 vacuum interferometer. In the far-infrared region (400–100 cm^{-1}), the vacuum bench apparatus was equipped with a 3.5-μm-thick Mylar beam splitter, a globar source, and a DTGS/PE far-infrared detector. JEOL, Transmission Electron Microscope (TEM), JEM-1230 was used to investigate the powders. Magnetic measurements (susceptibility and magnetization) were carried out with a fully automated magnetometer (MPMS-5S from Quantum Design) using an ultra-sensitive Superconducting QUantum Interference Device (SQUID) in the temperature range 4–300 K. A small piece of each glassy material was put into a small plastic vial, placed in a holder and finally inserted into the helium Dewar of the SQUID apparatus. The temperature dependence of the susceptibility data was recorded during heating of the sample using two modes: zero-field cooling (ZFC) and field cooling (FC), to determine the magnetic behavior. The procedure is based on performing two consecutive magnetization measurements: in the ZFC process, the sample is first cooled down in the absence of magnetic field, then the field is applied at 4.2 K, and the data of the magnetization M are recorded on increasing the temperature; in the FC process, the magnetic field is applied at room temperature, and the data are recorded upon decreasing the temperature. The magnetic field applied in such experiments was 10 kOe. On the other hand, magnetization curves $M(H)$ have been measured in the whole range $H \leq 30$ kOe. Magnetic data analyses were performed in CGS unit system.

2.3. De-intercalation and electrochemistry

Partial removal of lithium ions from the layered framework has been carried out by using potassium peroxydisulfate ($K_2S_2O_8$) in an aqueous solution. The mixture of $LiCo_{0.8}Mn_{0.2}O_2$:$K_2S_2O_8$ was dissolved in water and stirred at room temperature for 24 h. The powders were washed, filtered and dried at 200 °C.

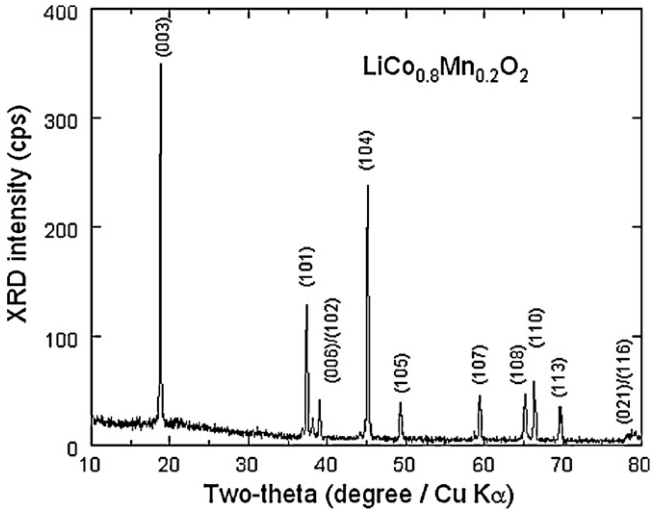

Fig. 1. X-ray diffraction patterns of $LiCo_{0.8}Mn_{0.2}O_2$ powders synthesized by wet chemistry method assisted by citric acid (calcinations temperature 800 °C).

The electrochemical properties of the product were tested at 25 °C in cells with metallic lithium as the negative electrode using Teflon laboratory-cell hardware and Mac-Pile system. The non-aqueous electrolyte was 1.0 mol L^{-1} $LiClO_4$ dissolved in propylene carbonate (PC). The active electrode material was deposited onto Al foil at the loading 8.8 mg cm^{-2}. Charge and discharge processes were carried out at rates of C/12 and C/6, respectively, in the voltage range 3.0–4.4 V vs. Li^0/Li^+ (we use the usual convention, after which 'C/n' means 'in n hours'). Ragone plot has been explored up to 10 C.

3. Results and discussion

3.1. Structure and morphology

$LiCoO_2$ has the trigonal crystal structure based on alternative ordering of Li and Co in the octahedral sites of the oxygen close packing. When Mn is substituted for Co in $LiCoO_2$ in an amount 0.2, the trigonal lattice is preserved. For manganese substitutive, the structure is almost ideal, i.e., the layered α-$NaFeO_2$-type structure ($R\bar{3}m$ space group). Fig. 1 shows the XRD patterns of $LiCo_{0.8}Mn_{0.2}O_2$, dominated by the main characteristic peaks (0 0 3), (1 0 1) and (1 0 4) planes at $2\theta \approx 19$, 37 and 45°. The diffraction patterns show a clear splitting of the hexagonal characteristic doublets (0 0 6)/(1 0 2) and (1 0 8)/(1 1 0). In conclusion the XRD pattern of the sample calcined at 800 °C for 24 h shows the formation of single-phased $LiCo_{0.8}Mn_{0.2}O_2$ chemically and structurally homogeneous, and all the peaks can be indexed according to the layered α-$NaFeO_2$ structure.

Table 1 gives XRD results obtained from $LiCo_{0.8}Mn_{0.2}O_2$ powders calcined at different temperatures. The hexagonal cell parame-

Table 1
XRD results obtained from $LiCo_{0.8}Mn_{0.2}O_2$ powders synthesized by wet chemistry assisted citric acid and calcined at 400, 600 and 800 °C. T is the calcinations temperature, a and c the lattice parameters of the hexagonal structure, V is the volume of the unit cell, and L is the size of the crystallites deduced from the Scherrer's law.

T (°C)	a (Å)	c (Å)	c/a	V (Å^3)	I_{003}/I_{104}	L (nm)
400	2.820(5)	14.06(5)	4.986	96.82	1.23	9.7
600	2.819(3)	14.06(3)	4.989	96.79	1.10	11.04
800	2.830(3)	14.12(3)	4.992	97.86	1.54	47.5

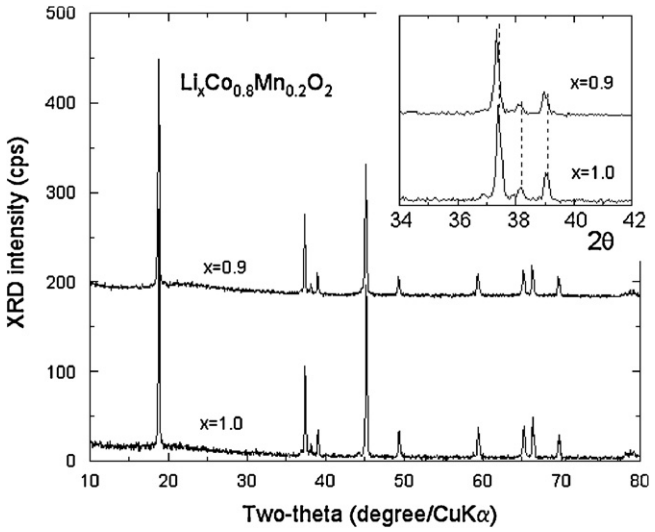

Fig. 2. X-ray diffraction patterns for pristine ($x = 1$) and chemically delithiated ($x = 0.9$) $Li_xCo_{0.8}Mn_{0.2}O_2$ synthesized by wet chemistry method assisted by citric acid and its lithiated form.

ters of the synthesized $LiCo_{0.8}Mn_{0.2}O_2$ at 800 °C are found to be $a = 2.83(3)$ Å, $c = 14.12(3)$ Å and $c/a = 4.992$, respectively. The substitution of Mn for Co expands the unit cell, which matches well with the ionic radii of Co^{3+} and Mn^{3+} of 0.53 and 0.63 Å, respectively. The c value increases with the calcination temperature, whereas the lattice constant a remains almost unchanged. The increase of the lattice constant c implies an enhancement of Li^+ ion diffusion in the layered structure [23]. Larger lattice parameter means that Li^+ ion can move easily in the compounds, which can increase the rate capability and indicates that the crystallinity is improved [24]. Indeed, the volume V of the unit cell also reported in Table 1 increases with the calcination temperature, which confirms the better crystallinity reached at 800 °C.

The intensity ratio I_{003}/I_{104} and the lattice parameter ratio c/a have been considered as an indication of the degree of cation mixing [25–27], the reason why it has also been reported as a function of calcination temperature in Table 1. It is found that the intensity ratios of the diffraction peaks increase with increasing temperature. The $I_{003}/I_{104} = 1.23$, 1.10 and 1.54 for the samples calcined at 400, 600 and 800 °C for 24 h, respectively. The ratio I_{003}/I_{104} has been used to measure the ordering of the two-dimensional layered $LiMO_2$ (M: Co, Mn) compounds related to a good electrochemical potential [28]. The value of $I_{003}/I_{104} < 1.2$ is an indication of undesirable ordering structure [29,30]. The reversible capacity is known to decrease when $I_{003}/I_{104} < 1.2$ and is completely inactive when $I_{003}/I_{104} < 1.0$ [31,32]. This is the case of the sample heated at 600 °C where the value of $I_{003}/I_{104} = 1.10$, giving evidence of a large cation-mixing. On the other hand, the large value of this ratio in the sample heated at 800 °C confirms its excellent structural properties.

Table 1 also shows the variation of the coherence length, i.e. the size L of the crystallites, in $LiCo_{0.8}Mn_{0.2}O_2$ prepared under various temperatures. L has been deduced from the Scherrer's formula [33]. Note the Scherrer's formula neglects the strain field effects, which is a reasonable approximation before delithiation, but we shall return to this approximation below.

Fig. 2 shows the XRD pattern of the sample $Li_xCo_{0.8}Mn_{0.2}O_2$ partially delithiated according to the procedure mentioned in Section 2, together with that of the same sample $LiCo_{0.8}Mn_{0.2}O_2$ before delithiation for comparison. The Rietveld refinements are shown in Fig. 3. Only one phase is present with sharp Bragg peaks indicating that the layered structure is maintained with a good crystallinity after the chemical de-intercalation. No evidence of Bragg peaks due

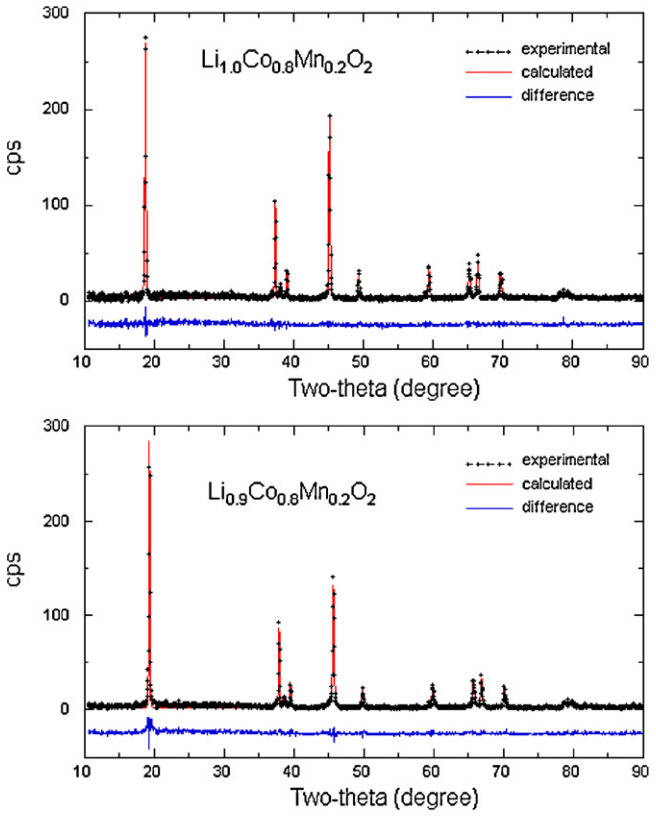

Fig. 3. Rietveld refinement of the X-ray diffraction patterns of the $Li_xCo_{0.8}Mn_{0.2}O_2$ samples.

to a phase transition or a second phase has been detected. The splitting between (1 0 8) and (1 1 0) gives evidence of a strengthening of 2D character in $Li_xCo_{0.8}Mn_{0.2}O_2$ upon lithium removal. The reliability index (R-factor) deduced from the Rietveld refinement reported in Table 2 is $R \sim 0.5$. It is considered as a good indicator of hexagonal ordering [32]. The composition deduced from the Rietveld refinement is $x \approx 0.9$. Local charge neutrality then implies that about half of the Mn ions are in the Mn^{4+} valence state, while the rest remains in the Mn^{3+} valence state. This will be confirmed by magnetic measurements in the next section.

Table 2 shows the variation of the lattice parameters upon delithiation. The lattice parameter a decreases, but the lattice parameter c increases, which results in an increase of the volume of the structure. This expansion of the inter-slab distance is associated with the cationic mixing of Mn^{4+} and Mn^{3+} ions in the $(Co_{0.8}Mn_{0.2})O_2$ slabs.

In general, several factors can contribute to the broadening of peaks in X-ray diffraction [34,35]. In the case of manganese compounds, we have already shown that two factors need being taken into account: the size of the crystallites and the strain field [36]. We then follow this previous work and combine the Scherrer's equation for crystallite size and the Bragg's law for diffraction to determine crystallite size L and micro-strain local $\langle e^2 \rangle$ by using the following equation:

$$B^2 \cos^2\theta = 16\langle e^2 \rangle \sin^2\theta + \frac{K^2\lambda^2}{L^2} \quad (1)$$

where B is the full-width at half-maximum (fwhm) in radian, after correction of the instrumental broadening for finely powdered silicon powder, θ is the diffraction angle and K is a near-unity constant related to crystallite shape. The plot of the first member as a function of $\sin^2\theta$ is reported in Fig. 4 for the pristine $LiCo_{0.8}Mn_{0.2}O_2$ and its delithiated product $Li_xCo_{0.8}Mn_{0.2}O_2$ ($x \approx 0.1$). The plots are well

Table 2
X-ray diffraction results obtained on lithiated $LiCo_{0.8}Mn_{0.2}O_2$ powders synthesized by wet chemistry assisted citric acid and calcined at 800 °C in comparison with its delithiated phase. The symbols are the same as in Table 1.

Samples	a (A°)	c (A°)	c/a	V (A°^{3})	L (nm)	Reliability index (R)
Lithiated $LiCo_{0.8}Mn_{0.2}O_2$	2.830(3)	14.11(5)	4.98	97.03	52	0.497
Delithiated $Li_xCo_{0.8}Mn_{0.2}O_2$	2.810(7)	14.14(3)	5.02	97.25	52	0.371

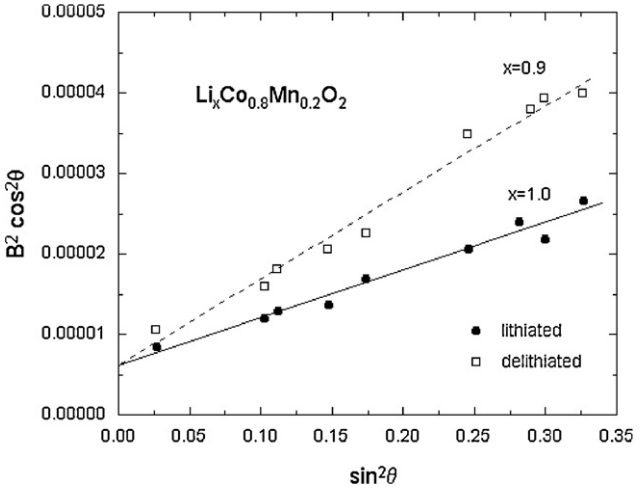

Fig. 4. Analysis of the full-width B at half-maximum of the XRD peaks according to Eq. (1). B is in radian.

fit by straight lines, in agreement with Eq. (1). The slope of the linear fit of the data provides us with the value of $\langle e^2 \rangle$, while the extrapolation to $\sin\theta = 0$ provides us with the value of the coherence length L.

Note that the linear law shown in the figure gives indirect evidence that L is independent of q. The crystallites are then spherical as first approximation, so that we take for the constant K the value appropriate to this particular case, $K = 0.9$. The spatial coherence length of samples of given composition may vary by a factor two from one sample to another, due to the impossibility of controlling all the numerous parameters during the synthetic process. Therefore, the dependence of L on y does not carry any significance. However, for all the samples we have investigated, we find $L \approx 60$ nm, within a factor two. This value of L is a typical value for intercalation compounds, not only for lamellar compounds [20]. On the other hand, the variations of L and $\langle e^2 \rangle$ for a given sample upon delithiation are meaningful. We find L is unaffected by the delithiation. For the sample in Fig. 4, we find $L = 52$ nm. On the other hand, we find that $\langle e^2 \rangle$ is affected by the delithiation process. Therefore, the lattice cannot accommodate the valence change of the Mn ions without generating local strain fields. This is the proof that the ions do not have the same ionic radius, i.e. are not in the same ionic state because the delithiation is incomplete. In case all the magnetic ions have the same ionic radius (case $x = 0$), the periodicity of the lattice would be maintained, so that the change $Mn^{3+} \rightarrow Mn^{4+}$ should be almost entirely accommodated by the global distortion of the lattice, i.e. the variations of the lattice parameters.

The morphology of $LiCo_{0.8}Mn_{0.2}O_2$ powders investigated by TEM is shown in Fig. 5. Powders are formed of well-dispersed particles, which are slightly agglomerated and display a small quantity of fragments. These TEM images are similar at any part of the samples, which appear to be homogeneous at a large scale. The average particle size of $LiCo_{0.8}Mn_{0.2}O_2$ is estimated to be in the range of 100 nm. The particle size deduced from TEM matches well with the coherence length deduced from XRD patterns, so that the primary particles are crystallites.

3.2. FTIR measurements

The XRD analysis does not allow us to determine the position of the Li atoms in the $LiCo_{0.8}Mn_{0.2}O_2$ structure because of the weak scattering of Li. Fourier transform infrared spectroscopy (FTIR) is known to be a good means of investigate of the structure at a local scale, and the nature of the cationic environment in the layered phase. IR features of $LiMO_2$ materials considering vibrations of compressed MO_6 and elongated LiO_6 octahedra that yield distinct modes in two different frequency regions. The stretching modes of $(Co,Mn)O_6$ octahedra occur in the high-frequency region (500–650 cm^{-1}), while the stretching mode of LiO_6 octahedra is observed in the far-infrared region around 250 cm^{-1} [37].

For $LiMO_2$ compounds, the four infrared active modes have been recorded at 266, 508, 555 and 598 cm^{-1} for $LiCoO_2$ and at 272, 450, 507 and 602 cm^{-1} for $LiMnO_2$. These vibrational features are consistent with the formation of the $LiCoO_2$–$LiMnO_2$ solid solution. The frequency position of the modes depends on the nature of the transition-metal ions (mass, ionic radius, oxidation state) [37]. The IR resonant frequency of LiO_6 groups appears at 266 and 272 cm^{-1} in the $LiCoO_2$ and $LiMnO_2$ layered structures ($R\bar{3}m$ space group), respectively. As far as the low-wavenumber peak

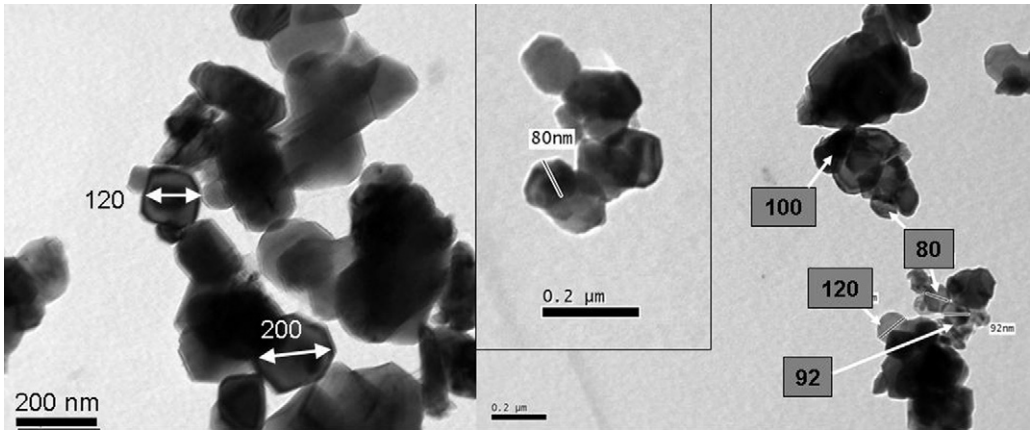

Fig. 5. TEM micrographs of $LiCo_{0.8}Mn_{0.2}O_2$ powders synthesized by wet-chemical method assisted by citric acid. Samples were calcined at 800 °C for 24 h in air.

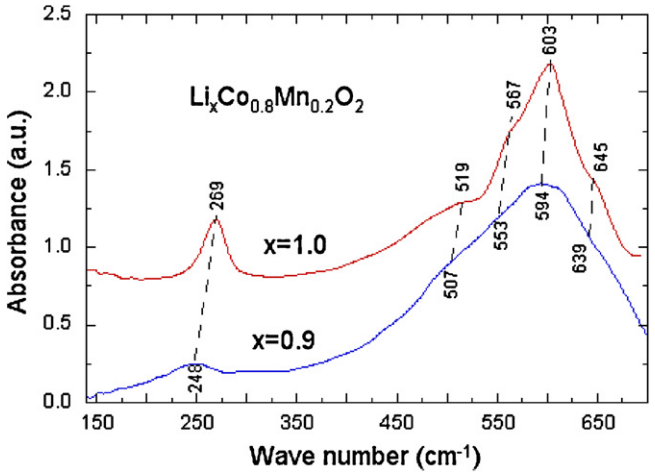

Fig. 6. FTIR absorption spectra of pristine $LiCo_{0.8}Mn_{0.2}O_2$ and delithiated $Li_xCo_{0.8}Mn_{0.2}O_2$ samples. Powders were synthesized by wet-chemical method assisted by citric acid and calcined at 800 °C for 24 h. Delithiated sample was obtained by immersion into a potassium peroxydisulfate solution.

is concerned, the isotopic Li replacement in $LiMO_2$ has proven that this IR band between 200 and 300 cm^{-1} is associated to the vibration of a relatively isolated LiO_6 octahedron [38]. Fig. 6 shows the room temperature FTIR absorption spectra of the layered $LiCo_{0.8}Mn_{0.2}O_2$ samples synthesized by wet chemistry method. As expected from the factor group analysis, these spectra display four distinct infrared bands. The IR band situated at 269 cm^{-1} is assigned with confidence to an asymmetric stretching vibration of the Li^+ ion with O^{2-} near neighbors in $LiCo_{0.8}Mn_{0.2}O_2$. However, a small mixing of Li–O stretching and O–*M*–O bending motion is present in the low-wavenumber peak. The high-frequency bands of the FTIR absorption spectra of $LiCo_{0.8}Mn_{0.2}O_2$ located at ca. 603 and 567 cm^{-1} are attributed to the asymmetric stretching modes of MO_6 group, whereas the low-frequency bands at ca. 519 cm^{-1} are assigned to the bending modes of O–*M*–O chemical bonds.

Fig. 6 illustrates the FTIR patterns of the $Li_xCo_{0.8}Mn_{0.2}O_2$ ($x \approx 0.9$) sample in comparison with the parent pristine sample. From the spectra shown in this figure we find that: (i) extracting Li ions does not change the space group, (ii) the frequency of LiO_6 octahedra is affected slightly by lithium de-intercalation, and (iii) displacement of the *M*–O stretching peaks occur. For example the slight frequency shift of LiO_6 vibrations from 269 to 248 cm^{-1} implies that the octahedral oxygen environment of Li^+ ions remains quite stable in the investigated concentration domain. This is related to the very small variation of the interslab distance (that corresponds to the *c*/*a* value for that hexagonal cell). The strength of the LiO_6 peak decreases upon Li extraction due to the decrease of the density of oscillators. The broadening of all the IR bands is associated with the disorder induced by the departure of Li ions located between two ($Co_{0.8}Mn_{0.2}$) blocks. In particular, the broadening of the low-frequency band is attributed to the random distribution of Li ions remaining in the host matrix. The frequency shift observed for the high-wave number bands that are assigned to the MO_2 layers is only small. Therefore, the MO_2 layers are not strongly affected by the lithium de-intercalation process.

3.3. Magnetic properties

Fig. 7 displays the isothermal magnetization curves *M*(*H*) in the range $4 \le T \le 300$ K for the $LiCo_{0.8}Mn_{0.2}O_2$ pristine material. Except at the lowest temperature (4.2 K), the magnetization is linear in *H*, which allows us to define the magnetic susceptibility by the formula $\chi_m = M/H$. Fig. 8 shows the temperature dependence of

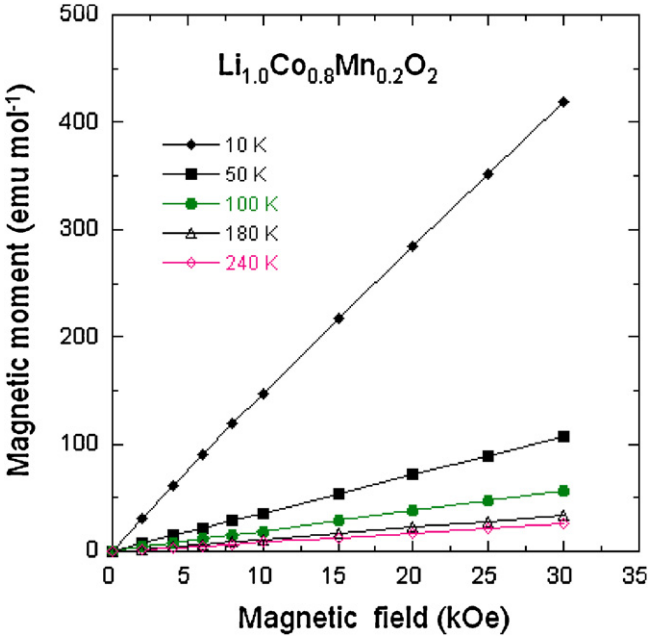

Fig. 7. Isothermal plots of the magnetization *M*(*H*) for $LiCo_{0.8}Mn_{0.2}O_2$ powder synthesized by wet-chemical technique assisted by citric acid pristine material ($x = 1.0$).

the reciprocal magnetic susceptibility of $LiCo_{0.8}Mn_{0.2}O_2$, $\chi_m^{-1}(T)$, which indicates that the Curie–Weiss law $\chi_m = C_p/(T-\theta)$ is satisfied down to approximately 50 K. No ordering is observed down to 10 K, the small downward curvature responsible for the departure of $\chi_m^{-1}(T)$ from the Curie–Weiss law below 50 K being easily accounted for by a residual contribution of localized spins. Such loose spins add a Curie contribution to the total susceptibility that diverges at $T = 0$ and is thus non-negligible below 50 K, even if their concentration is very small (0.01%). In the whole range $T \ge 10$ K, no difference could be detected between field-cooled and zero-field cooled susceptibilities (see Section 2), which is another evidence that the sample is paramagnetic in this whole range of temperatures. The linear fit of the $\chi_m^{-1}(T)$ curve at $T > 50$ K gives the paramagnetic Curie temperature $\theta_p = -14$ K and the Curie constant $C_p = 0.21$ emu K mol^{-1}. The effective moment per magnetic moment of the manganese ions deduced from C_p is $\mu_{eff} = 2.90\,\mu_B$. This is in

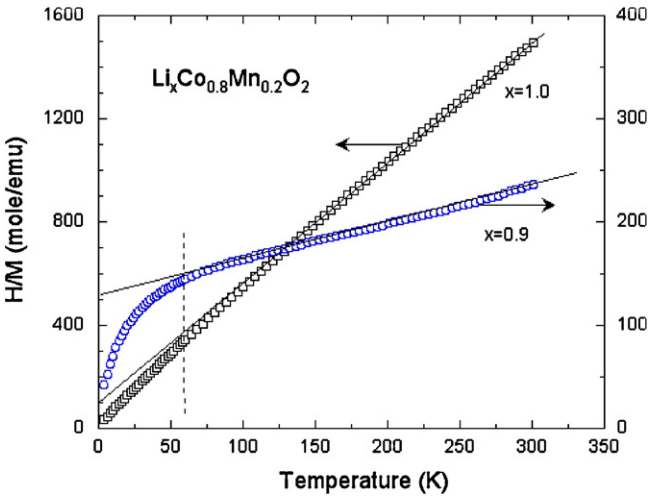

Fig. 8. Plot of *H*/*M* measured at $H = 10$ kOe for pristine $LiCo_{0.8}Mn_{0.2}O_2$ powder (left scale) and its delithiated parent $Li_xCo_{0.8}Mn_{0.2}O_2$ with $x = 0.23 \pm 0.02$ (right scale). Lithium extraction was performed by immersion of sample using the potassium peroxydisulfate method at room temperature.

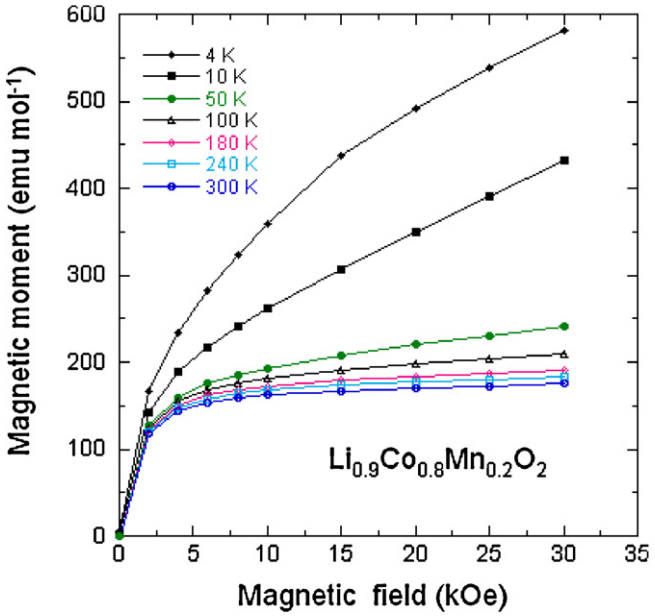

Fig. 9. Isothermal plots of the magnetization $M(H)$ for $Li_xCo_{0.8}Mn_{0.2}O_2$ powder synthesized by wet-chemical technique assisted by citric acid, after partial delithation by immersion into a potassium peroxydisulfate solution.

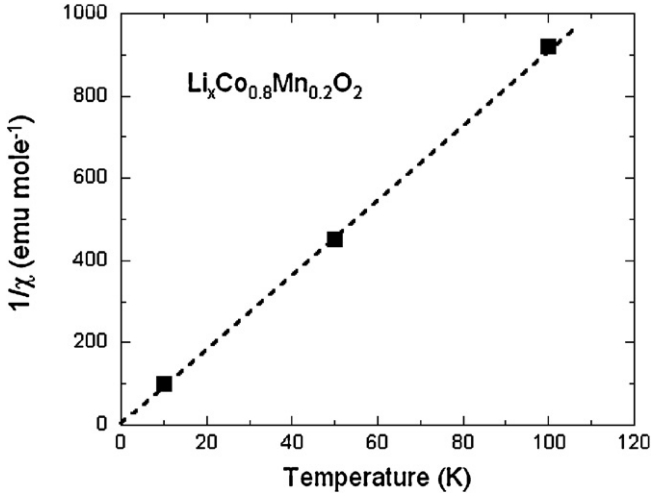

Fig. 10. Temperature dependence of the inverse of the magnetic susceptibility defined as dM/dH at $H > 15$ kOe for $Li_xCo_{0.8}Mn_{0.2}O_2$ powder synthesized by wet-chemical technique assisted by citric acid, after partial delithation by immersion into a potassium peroxydisulfate solution.

good agreement with the theoretical value 2.83 μ_B predicted by assuming that Mn is trivalent in the low-spin state ($t^4{}_{2g}e^0$, spin $S = 1$), while Co is in the Co^{3+} (non-magnetic) valence state.

In the low-temperature region, $LiCo_{0.8}Mn_{0.2}O_2$ exhibits a spin freezing at 8 K as evidenced by the cusp in the graph $\chi_m T$ vs. T (not show here) and below this temperature, a separation between field-cooled and zero-field cooled experiments, so that 8 K is also the temperature for the onset of magnetic irreversibility. The investigation of this spin freezing at very low temperatures, however, is beyond the scope of this work, and has been discussed elsewhere in intercalation compounds [39].

The low-spin state of Mn^{3+} shows that the transition to the high-spin state associated with a large variation of the volume of the unit cell due to the Jahn–Teller distortion in some other compounds [38–41] is not observed here. The intra-chain Mn–O–Mn 90° interaction will involve the empty d_{x2-y2} orbital and is expected to be weakly ferromagnetic (FM). The intra-chain Mn^{3+}–Mn^{3+} interaction occur via the half- filled $t_{2g}(d_{xz})$ orbitals across a shared octahedral-site edge and is antiferromagnetic (AFM), according to the Goodenough [42] and Kanamori [43] rules. The magnetic interactions are then a mixture of FM and AFM interactions generating frustration. The negative value of θ_p, however, reveals that AFM interactions are dominant. However, the Mn^{3+}–Mn^{3+} interactions are small, as shown by the small value of θ, which is consistent with the fact that the range of validity of the Curie–Weiss law extends down to 50 K.

The magnetization curves of the delithiated $Li_xCo_{0.8}Mn_{0.2}O_2$ sample are shown at different temperatures in Fig. 9. These curves are now far from linear, which makes the analysis more complex. First, we note that the magnetization can be decomposed, at least above 10 K, into a linear component, superposed on a component that saturates above 15 kOe, so that we can write

$$M \quad (H > 15\,\text{kOe}) = M_S + \chi^H \tag{2}$$

The magnetic susceptibility χ is now given by the slope of the magnetization curve in its linear part at high field. The plot of χ^{-1} as a function of T in Fig. 10 shows that it satisfies the Curie–Weiss law with a Curie temperature that is about the same as in the pristine sample before delithiation, so that this contribution has the same origin, namely the Mn^{3+} ions still present in the material, due to the incomplete delithiation. From the slope of $\chi^{-1}(T)$ we find the Curie constant $C_p = 0.11$ emu K mol^{-1}, twice smaller than that of the pristine sample. The concentration of Mn^{3+} ions that contribute to χ^H is then reduced by a factor 2, which amounts to 0.1 Mn^{3+} per mole of product. The other half of the manganese ions arise from the conversion of Mn^{3+} in Mn^{4+} associated with the partial delithiation. The intrachain 180° cation-oxygen-cation superexchange between octahedral site cations is antiferromagnetic according to the Goodenough–Kanamori rules for one cation in the d^4:$t^4{}_{eg}e^0{}_{eg}$ configuration (Mn^{3+}) and one ion in the $t^3{}_{eg}e^0{}_{eg}$ (Mn^{4+}). In addition, while the Mn^{3+}–Mn^{3+} interactions are small, the Mn^{3+}–Mn^{4+} interactions are strong, so that these pairs are spin frozen in an antiferromagnetic (AF) state. M_S is then the result of the uncompensated magnetic moment between the spins $S(Mn^{3+}) = 1$ and $S(Mn^{4+}) = 3/2$ forming N_{Mn} antiferromagnetic (AF) pairs

$$M_S = N_{Mn}\, g\mu_B[S(Mn^{4+}) - S(Mn^{3+})] = N_{Mn}\mu_B \tag{3}$$

with $g = 2$ the gyromagnetic factor. The extrapolation of the linear part of the total magnetization from high field down to $H = 0$ at $T > 50$ K gives $M_S \approx 160$ emu mol^{-1}. Inserting this value in Eq. (3), we find $N_{Mn} = 0.03$ per mole of product. Mn^{4+}–Mn^{4+} interactions are also antiferromagnetic according to the Goodenough–Kanamori rules, and strong. Therefore, we attribute to Mn^{4+}–Mn^{4+} AF pairs the difference between the total concentration 0.2 of manganese and the 0.16 Mn that contribute to Eq. (2) (0.1 unpaired Mn^{3+}, plus 0.03 Mn^{3+} and 0.03 Mn^{4+} forming Mn^{3+}–Mn^{4+} AF pairs). The total concentration of Mn^{3+} ions is 0.13, while the concentration of Mn^{4+} ions is 0.07. The electric charge neutrality then implies that the concentration of lithium is $x = 0.93$, in quantitative agreement with the result of Rietveld refinement (see Section 3.1). The ability of magnetic measurements to determine independently not only the total concentration x of Mn^{4+} ions, but also the concentration of Mn^{3+}–Mn^{4+} pairs and the Mn^{4+}–Mn^{4+} comes from the fact that the contribution of these entities to the magnetic properties is quite different. The Mn^{3+} ions are only weakly coupled to the other Mn^{3+} ions, so that Mn^{3+}–Mn^{3+} pairing is responsible for the Curie–Weiss contribution to the magnetization, responsible for the slope of the $M(H)$ curves at high field. The Mn^{4+} ions are strongly coupled to the other manganese ions, so that Mn^{4+}–Mn^{3+} pairs form a ferrimagnetic percolating structure responsible for the part of the magnetization that saturates to M_S at intermediate fields, while

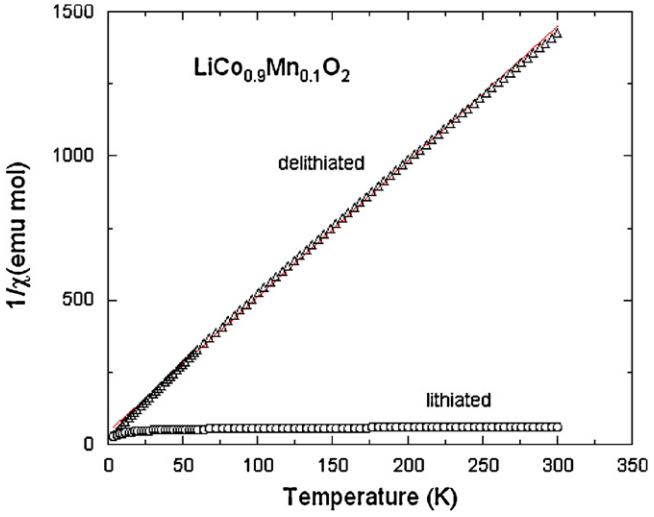

Fig. 11. Inverse of the magnetic susceptibility of $Li_xCo_{0.9}Mn_{0.1}O_2$ (same preparation process as for the $Li_xCo_{0.8}Mn_{0.2}O_2$ sample).

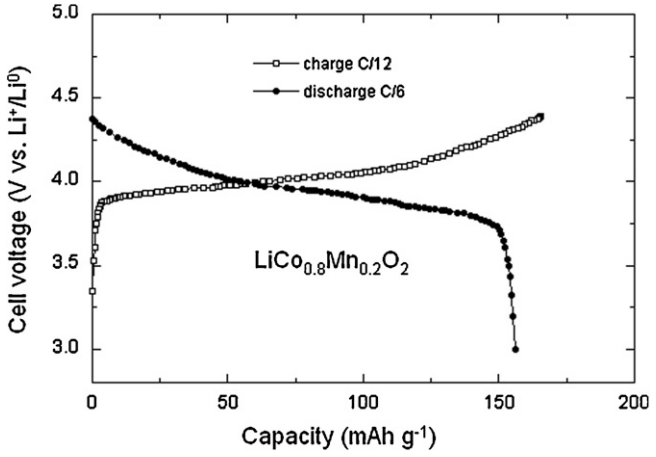

Fig. 12. Typical charge–discharge profiles of $Li//LiCo_{0.8}Mn_{0.2}O_2$ non-aqueous lithium cell employing the electrolyte of composition 1.0 mol L^{-1} $LiClO_4$ in PC at room temperature. Charge and discharge were carried out at current density C/12 and C/6 respectively.

Mn^{4+}–Mn^{4+} pairs are spin frozen in an AF configuration so that they do not contribute to the magnetization.

The chemical oxidation has thus allowed us to oxidize essentially half of the Mn ions. Note that the concentration of manganese involved in Mn^{4+}–Mn^{4+} is 0.04, meaning 0.02 AF pairs close to N_{Mn}, the difference 0.01 being typically within the uncertainty; the uncertainty in the concentrations of the AF pairs and of unpaired Mn^{3+} is typically 5×10^{-3}. This is actually expected since half of the Mn^{3+} converted in Mn^{4+} also means an equal concentration of Mn^{3+}–Mn^{4+} pairs and Mn^{4+}–Mn^{4+} pairs, so that there is a self-consistency between the results we have found for unpaired Mn^{3+} and AF pairs. The valence of the cobalt has not changed in the process, because electrochemical properties show the Mn ions are oxidized first, while Co^{3+} is oxidized in Co^{4+} only at high potential above 4 V as we shall see in the next section. This difficulty to change the oxidation state of Co from Co^{3+} to Co^{4+} is the reason why the limit $x = 0$ in $Li_xCo_{1-y}Mn_yO_2$ could be reached only in the absence of cobalt ($y = 1$), as reported in our previous work [11].

For comparison, we have made the same analysis on $LiMn_{0.1}Co_{0.9}O_2$. Because of the lower content in manganese, we do not have Mn–Mn pairing in that case, and this is shown by the magnetic properties, the analysis of which is now very simple: the magnetization in that case is linear in H before and after the partial delithiation using the same chemical procedure (same product, same time). The inverse of the susceptibility curves $\chi^{-1}(T)$ before and after the chemical delithiation are shown in Fig. 11. $\chi^{-1}(T)$ for the pristine sample does not follow the Curie–Weiss-law; it is due to the superposition of the Curie–Weiss-law owing to the Mn^{3+} ions and the temperature independent contribution of the Co^{3+} ions responsible for a Van-Vleck paramagnetism that we have investigated elsewhere [44]. The quantitative analysis of the $\chi^{-1}(T)$ curve in that case is similar to that of $LiCoO_2$ with magnetic impurities [45]. Let us focus here on the $\chi^{-1}(T)$ curve of the partially delithiated sample. The Curie–Weiss contribution of the magnetic ions is now dominant, because of the conversion of Mn^{3+} in Mn^{4+} that carries a larger spin. Indeed, the Curie constant C_p is found equal to 0.217, which is larger than the value expected assuming that all the Mn ions are in the Mn^{4+} valence state. Taking into account that Co^{4+} carries a spin 5/2, we find that the conversion of 2% of the cobalt in Co^{4+} valence state is sufficient to account for the experimental value of C_p, which means 0.018 positive charge per chemical formula, that adds to the 0.1 charge due to the conversion of Mn^{3+} in Mn^4. This excess of positive charge must to be compensated by the removal of Li^+, so that x in $Li_xMn_{0.1}Co_{0.9}O_2$ is 0.88. Note that this value of x is close to that of the delithiated $Li_xMn_{0.2}Co_{0.8}O_2$. However, to reach this value in the case of $Li_xMn_{0.1}Co_{0.9}O_2$, we had to convert all the Mn^{3+} ions in Mn^{4+}, while in $Li_xMn_{0.1}Co_{0.9}O_2$, half of them only were oxidized. We can then infer from this comparison that the chemical process solution used to delithiate the material allows for a removal of 0.10 ± 0.03 lithium per $Li_xCo_{1-y}Mn_yO_2$ formula provided that the manganese concentration is large enough (i.e. $y \geq 0.1$). For $y < 0.1$, we shall have $x \approx y$ due to the difficulty to oxidize the cobalt by this chemical process.

3.4. Electrochemical studies on $LiCo_{0.8}Mn_{0.2}O_2$

The variation of potential of $LiCo_{0.8}Mn_{0.2}O_2$ electrode calcined at 800 °C for 24 h is shown in Fig. 12. There is a good reproducibility of charge–discharge curves. The discharge capacity obtained from Fig. 12 and in Table 3 is 156.7 mAh g^{-1} when discharged to a cut-off voltage of 2.7 V, with a discharge efficiency of 92.7%. About 12 mAh g^{-1} irreversible capacity was observed during the first charge and discharge. This result is in a good agreement with previously reported work by Suresh et al. [46]. The shape of the charge–discharge curves shows a good reversibility during the first cycle. In the composition domain $0 \leq x \leq 0.6$ the voltage charge profile of the $Li//LiCo_{0.8}Mn_{0.2}O_2$ cells exhibited an increase of the potential followed by a plateau at ca. 3.85 V. The voltage profiles exhibited a quasi-flat domain at about 3.85 V followed by a potential increase for a depth of charge $x > 0.4$ and reached 4.3 V at $x = 0.55$. The first plateau, near 3.85 V, is due to the oxidation of Mn^{3+} ions, while at $x > 0.5$ the profiles were very close to those of the $Li//Li_xCoO_2$ cell. These features are also apparent in Fig. 13 depicting the differential capacity ($-\partial Q/\partial V$) vs. cell potential. Thus, the second stage near 4.0 V is attributed to oxidation of Co^{3+} ions. These resulted from the prior oxidation of Mn^{3+} ions before the cobalt ions. Fig. 14 shows that the capacity is reduced by a factor 2 at 10 C rate, and that no significant loss of capacity is observed

Table 3
Initial discharge capacity, charge capacity and discharge efficiency % of $LiCo_{0.8}Mn_{0.2}O_2$.

Sample	$LiCo_{0.8}Mn_{0.2}O_2$	x in $Li_xCo_{0.8}Mn_{0.2}O_2$
Discharge capacity (mAh g^{-1})	157	0.57
Charge capacity (mAh g^{-1})	169	0.61
Discharge efficiency %	93	93

Discharge efficiency % = discharge capacity/charge capacity.

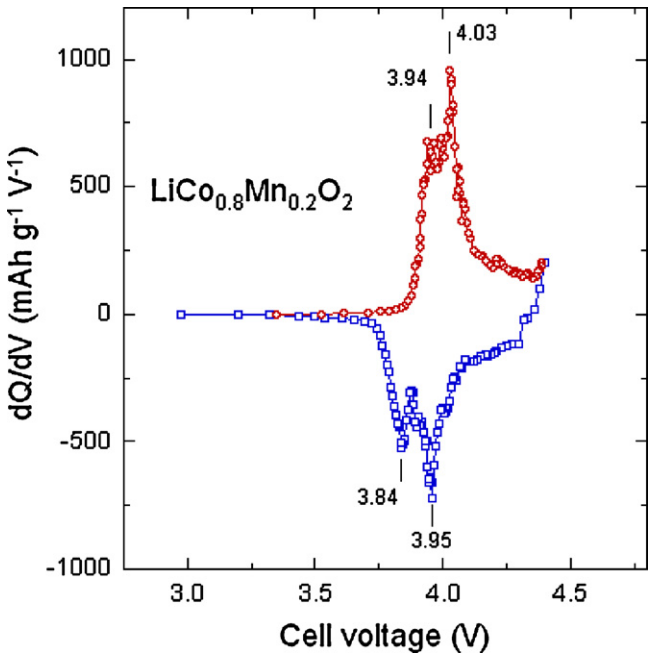

Fig. 13. Differential capacity ($-\partial Q/\partial V$) vs. cell potential of the Li//$LiCo_{0.8}Mn_{0.2}O_2$ experimental cell presented in Fig. 11. Charge and discharge were carried out at current density C/12 and C/6, respectively, like in Fig. 12.

during the 30 cycles for which it was tested. The capacity at 1 C rate is 134 mAh g^{-1}. This performance was not necessarily expected for this material, since Mn^{3+} is a Jahn–Teller ion, which implies that the change of valence $Mn^{3+} \Leftrightarrow Mn^{4+}$ is accompanied by local distortions, and thus strain fields, which reduces the life of the battery, especially at high C-rates. The generation of strain fields is well observed in our samples (see Section 2). We have noticed, however, that this strain field was not sufficient to generate spin transitions between low and high spin states for the manganese ions, in contrast with what we have observed in other compounds such as $LiMnPO_4$ in particular [47]. One reason is that the concentration of Mn ions is limited to 0.2, and indeed, at such dilutions, such spin transitions and the dramatic loss of the electrochemical properties are avoided in $LiFe_{1-y}Mn_yPO_4$. The absence of spin transition in $LiCo_{1-y}Mn_yO_2$ presumably plays a role in the results we have obtained in the present work.

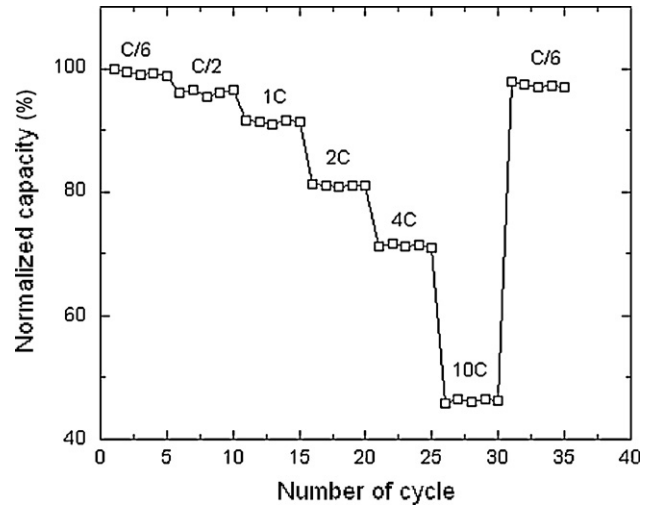

Fig. 14. Cycling performance of Li//$LiCo_{0.8}Mn_{0.2}O_2$ cells at various current densities between 3.0 and 4.4 V vs. Li^+/Li^0.

4. Conclusions

The lithium extraction–insertion reactions have been explored in a $Li_xCo_{0.8}Mn_{0.2}O_2$ matrix having the rhombohedral symmetry. The immersion of $LiCo_{0.8}Mn_{0.2}O_2$:$K_2S_2O_8$ dissolved in water and stirred at room temperature for 24 h removes 0.10 ± 0.03 lithium per $LiCo_{0.8}Mn_{0.2}O_2$ formula, and this is actually true also for different substitution rates of Co for Mn, which shows the ability of Mn^{3+} ions to oxidize. Magnetic experiments turned out to be a very powerful tool to analyze the delithiation process. It allowed us to determine the composition *x*, i.e. the rate of delithiation, which is found in quantitative agreement with the value deduced from the Rietveld refinement of the XRD spectra. In addition, it allowed us to determine that the chemical delithiation proceeds only by oxidation of Mn^{3+} in Mn^{4+}, while the cobalt remains in the trivalent state. This result is consistent with the results of electrochemical experiments, according to which the oxidation of Co^{3+} takes place only in a second step, at high voltage near 4.0 V. The chemical delithiation process is too soft to reach this second step. In addition, the magnetic experiments allowed us to extract information that Rietveld refinements fail to give, such as the concentrations of Mn^{3+}–Mn^{3+}, Mn^{3+}–Mn^{4+}, and of Mn^{4+}–Mn^{4+} nearest neighbors. The results reveal an homogeneous distribution of manganese in the metal ion sublattice, which is consistent with the good crystallization and good homogeneity probed at the mesoscopic scale by the FTIR experiments. The electrochemical properties under such conditions show that this low-temperature cathode material exhibits acceptable electrochemical capacity with lower polarization, operating at potentials below 4 V.

References

[1] K. Mizushima, P.C. Jones, J.B. Goodenough, Mater. Res. Bull. 15 (1980) 783–789.
[2] M.M. Thackeray, W.I.F. David, P.G. Bruce, J.B. Goodenough, Mater. Res. Bull. 18 (1983) 461–472.
[3] M.G.S.R. Thomas, W.I.F. David, J.B. Goodenough, Mater. Res. Bull. 20 (1985) 1137–1146.
[4] P.G. Bruce, A.R. Armstrong, H.T. Huang, J. Power Sources 68 (1997) 19–23.
[5] A.R. Armstrong, P.G. Bruce, Nature 381 (1996) 499–500.
[6] A.K. Padhi, K.S. Nanjundaswamy, J.B. Goodenough, J. Electrochem. Soc. 144 (1997) 1188–1194.
[7] A. Ait-Salah, A. Mauger, K. Zaghib, J.B. Goodenough, N. Ravet, M. Gauthier, F. Gendron, C.M. Julien, J. Electrochem. Soc. 153 (2006) A1692–A1701.
[8] M. Balasubramanian, X. Sun, X.Q. Yang, J. McBreen, J. Electrochem. Soc. 147 (2000) 2903–2909.
[9] T. Ohzuku, Y. Makimura, Chem. Lett. 8 (2001) 744–745.
[10] C.M. Julien, A. Amdouni, S. Castro-Garcia, M. Selmane, S. Rangan, Mater. Sci. Eng. B 128 (2006) 138–150.
[11] A. Abdel-Ghany, K. Zaghib, F. Gendron, A. Mauger, C.M. Julien, Electrochim. Acta 52 (2006) 4092–4100.
[12] T. Ohzuku, Y. Makimura, Chem. Lett. (2001) 642–643.
[13] Y. Makimara, T. Ohzuku, J. Power Sources 119–121 (2003) 156–160.
[14] S.H. Kang, K. Amine, J. Power Sources 119–121 (2003) 150–155.
[15] A. Abdel-Ghany, K. Zaghib, A. Mauger, F. Gendron, A.E. Eid, H. Abbas, A.M. Hashem, C.M. Julien, ECS Trans. 3 (27) (2007) 131–135.
[16] A. Abdel-Ghany, K. Zaghib, A. Mauger, M. Massot, F. Gendron, C.V. Ramana, C.M. Julien, ECS Trans. 3 (36) (2007) 119–123.
[17] A. Abdel-Ghany, A. Mauger, F. Gendronl, K. Zaghib, C.M. Julien, ECS Trans. 3 (36) (2007) 137–141.
[18] K. Ben Kamel, N. Amdouni, A. Abdel-Ghany, K. Zaghib, A. Mauger, F. Gendron, C.M. Julien, Ionics 14 (2008) 89–97.
[19] R. Stoyanova, E. Zhecheva, L. Zarkova, Solid State Ionics 73 (1994) 233–240.
[20] P. Suresh, P. Suresh, S. Rodrigues, A.K. Shukla, H.N. Vasan, N. Munichandraiah, Solid State Ionics 176 (2005) 281–290.
[21] S.-H. Na, H.-S. Kim, J.-H. Chin, S.-I. Moon, 204th Meeting of the Electrochemical Soc. Abs. 182 (2003).
[22] A. Caballero, L. Hernan, J. Morales, E.R. Castellon, J. Santos, J. Power Sources 128 (2004) 286–291.
[23] P. Kalyani, N. Kalaiselvi, N.G. Renganathan, M. Raghavan, Mater. Res. Bull. 39 (2004) 41–54.
[24] Y.-J. Huang, D.-S. Gao, G.-T. Lei, Z.-H Li, G.-Y. Su, Mater. Chem. Phys. 106 (2007) 354–359.
[25] S.H. Oh, W.T. Jeong, W.I. Cho, B.W. Cho, K. Woo, J. Power Sources 140 (2005) 145–150.
[26] I. Saadoune, C. Delmas, J. Solid State Chem. 136 (1998) 8–15.

[27] R.K.B. Gover, M. Yonemura, A. Hirano, R. Kanno, Y. Kawamoto, C. Murphy, B.J. Mitchell, J.W. Richardson Jr., J. Power Sources 81–82 (1999) 535–541.
[28] C. Julien, L. El-Farh, S. Rangan, M. Massot, J. Sol–Gel Sci. Technol. 15 (1999) 63–72.
[29] K.M. Shaju, G.V. Subba Rao, B.V.R. Chowdari, Electrochim. Acta 48 (2002) 145–151.
[30] T. Ohzuku, A. Ueda, M. Nagayama, Y. Iwakoshi, H. Komori, Electrochem. Acta 38 (1993) 1159–1167.
[31] D. Aurbach, K. Gamolsky, B. Markovsky, G. Salitra, Y. Gofer, U. Heider, R. Oesten, M. Schmidt, J. Electrochem. Soc. 147 (2000) 1322–1331.
[32] J.N. Reimers, J.R. Dahn, J.E. Greedan, C.V. Stager, G. Liu, I. Davidson, U. Von Sacken, J. Solid State Chem. 102 (1993) 542–552.
[33] B.D. Cullity, Elements of X-ray Diffraction, 2nd ed., Addison Wesley, Reading, MA, 1978, p. 102.
[34] H.P. Klug, L.E. Alexander, X-ray Diffraction Procedures for Polycrystalline and Amorphous Materials, Wiley, New York, 1974.
[35] C. Hammond, The Basic of Crystallography and Diffraction, Oxford University Press, New York, 1997.
[36] N. Amdouni, F. Gendron, A. Mauger, H. Zarrouk, H.C.M. Julien, Mater. Sci. Eng. B 129 (2006) 64–75.
[37] C. Julien, Solid State Ionics 136–137 (2000) 887–896.
[38] P. Tarte, J. Preudhomme, Spectrochim. Acta A 26 (1970) 747.
[39] C.M. Julien, A. Mauger, A. Vijh, K. Zaghib, Materials Science for Energy Storage, Anna University Press, Chennai, 2010.
[40] K. Numata, C. Sakaki, S. Yamanaka, Solid State Ionics 117 (1999) 257–263.
[41] A.S. Wills, N.P. Raju, C. Morin, J.E. Greedan, Chem. Mater. 11 (1999) 1936–1941.
[42] J.B. Goodenough, Magnetism and the Chemical Bond, Wiley, New York, 1963.
[43] J. Kanamori, J. Phys. Chem. Solids 10 (1959) 87–98.
[44] A. Mauger, D. Scalbert, J. Gaj, C. Benoit à la Guillaume, Phys. Rev. B 43 (1991) 7102–7108.
[45] C.M. Julien, A. Mauger, H. Groult, X. Zhang, F. Gendron, Chem. Mater. 23 (2011) 208–218.
[46] P. Suresh, S. Rodrigues, A.K. Shukla, H.N. Vasan, N. Munichandraiah, Solid State Ionics 176 (2005) 281–290.
[47] M. Kopec, A. Yamada, G. Kobayashi, S. Nishimura, R. Kanno, A. Mauger, F. Gendron, C. Julien, J. Power Sources 189 (2009) 1154–1163.